Elastic flexure controls magma trajectories and explains the offset of primary volcanic activity upstream of mantle plume axis at la Réunion and Hawaii hotspot islands

Muriel Gerbault [a,*], Fabrice J. Fontaine [b], Michel Rabinowicz [a], Misha Bystricky [c]

[a] Géosciences Environnement Toulouse – CNRS, IRD, Université de Toulouse, Observatoire Midi-Pyrénées, F31400 Toulouse, France
[b] Institut de Physique du Globe de Paris, CNRS, Université Paris 7, Observatoire Volcanologique du Piton de la Fournaise, Île de la Réunion, France
[c] IRAP – CNRS, Université de Toulouse, Observatoire Midi-Pyrénées, F31400 Toulouse, France

ARTICLE INFO

Keywords:
hotspot
flexure
compression
volcanism
visco-elasticity
la Réunion

ABSTRACT

Surface volcanism at la Réunion and Hawaii occurs with an offset of 150–180 km upstream to the plume axis with respect to the plate motion. This striking observation raises questions about the forcing of plume-lithosphere thermo-mechanical interactions on melt trajectories beneath these islands. Based on visco-elasto-plastic numerical models handled at kilometric resolution, we propose to explain this offset by the development of compressional stresses at the base of the lithosphere, that result from elastic plate bending above the upward load exerted by the plume head. This horizontal compression adopts a disc shape centered around the plume axis: (i) it is 20 km thick, (ii) it has a 150 km radius, (iii) it lays at the base of the elastic part of the lithosphere, i.e., around ∼50–70 km depth where the temperature varies from ∼600 °C to ∼750 °C, (iv) it lasts for 5 to 10 My in an oceanic plate of age greater than 70 My, and (vi) it is controlled by the visco-elastic relaxation time at ∼50–70 km depth. This period of time exceeds the time during which both the Somalian/East-African and Pacific plates drift over the Reunion and Hawaii plumes, respectively. This indicates that this basal compression is actually a persistent feature. It is inferred that the buoyant melts percolating in the plume head pond below this zone of compression and eventually spread laterally until the most compressive principal elastic stresses reverse to the vertical, i.e., ∼150 km away from the plume head. There, melts propagate through dikes upwards to ∼35 km depth, where the plate curvature reverses and ambient compression diminishes. This 30–35 km depth may thus host a magmatic reservoir where melts transported by dykes pond. Only after further magmatic differentiation can dykes resume their ascension up to the surface and begin forming a volcanic edifice. As the volcano grows because of melt accumulation at the top of the plate, the lithosphere is flexed downwards, inducing extra tensile stress at 30–35 km depth and compression at ∼15 km depth (induced by the edifice load). It implies that now the melts pond at ∼15 km and form another magmatic reservoir lying just underneath the crust. These processes explain the ponding of primary (shield) melts at ∼35 km and ∼15 km depths as recorded below La Reunion, Mauritius or Hawaii volcanoes, all shifted by ∼150 km with respect to the plume axis.

1. Introduction

Recent imaging of mantle plumes at Réunion and Hawaii reveals a striking offset of the most recent volcanoes upstream from the plume axis: at la Réunion, this offset was detected from Barruol and Fontaine (2013)'s analysis of SKS wave splitting. The observed pattern of azimuthal anisotropy is found compatible with a simple model of sub-lithospheric spreading of La Réunion plume above an axis located 150–180 km North–East of the Réunion Island (Fig. 1). Beneath the Hawaiian hotspot as well, analysis of P-wave velocities and He signatures (Hanyu et al., 2005; Ballmer et al., 2013, and reference therein) reveals that some of the most recent sites of volcanic activity are actually offset upstream by about 180 km from the slowest anomaly at 200 km depth (<1 Ma, the Loihi offshore volcanic system is located 20 miles southeast of Hawaii's big island). The present study focuses on the Réunion case, but we will also mention regularly the Hawaiian case when appropriate.

Morgan (1981) proposed that the Réunion "hotspot" was the manifestation of a deep mantle plume, whose track on the

* Corresponding author.
E-mail address: muriel.gerbault@get.omp.eu (M. Gerbault).

http://dx.doi.org/10.1016/j.epsl.2017.01.013

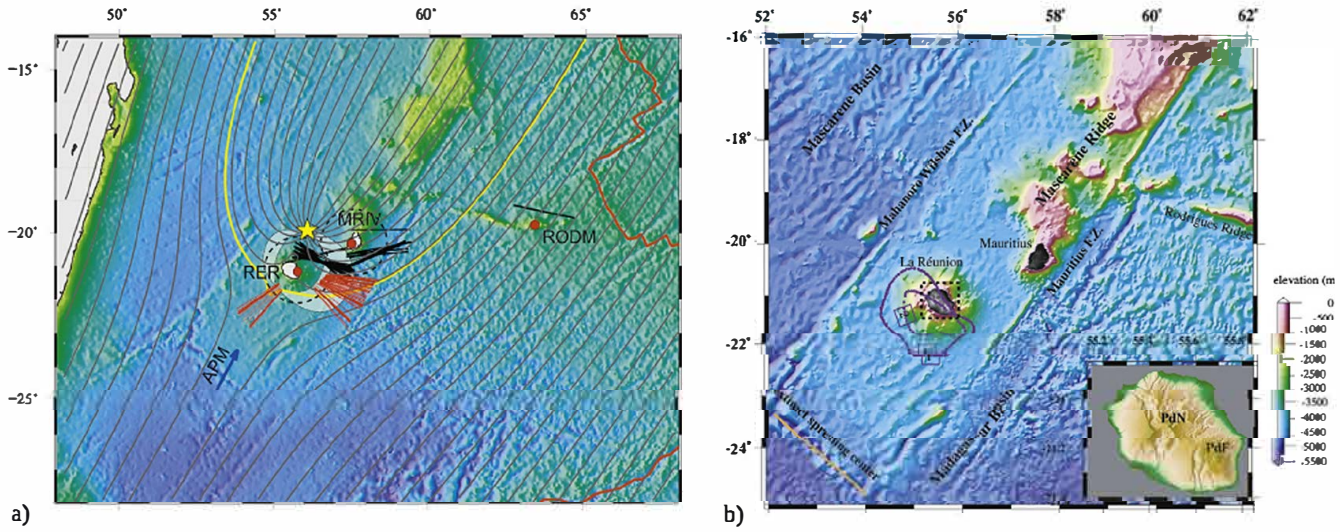

Fig. 1. La Réunion hotspot: a): SKS mantle anisotropy orientations (red and black lines) consistent with stream-lines orientations (gray plain lines) deduced from a standard mantle-plume model centered below the yellow star (from Barruol and Fontaine, 2013), indicating its ~150–200 km offset with respect to surface volcanism at the Réunion and Mauritius islands. RER (Réunion), MRV (Mauritius) and RODM (Rodrigues) are the names of the island-based seismometers. b) Bathymetric map of La Reunion area, modified from Fontaine et al. (2015): topography data displaying fracture zones (FZ) and ridges, isocontours of the thickness of underplated magmatic body beneath La Réunion indicated in purple deduced from wide-angle seismic lines (Gallart Muset et al., 1999). The inlet displays the location of the Piton de la Fournaise volcano (PdF) and Piton des Neiges (PdN) on the Island. (For interpretation of the references to color in this figure legend, the reader is referred to the web version of this article.)

northward-moving East-African/Somalian plate is represented by Réunion and Mauritius islands and the Mascarene Plateau. Volcanic activity on Mauritius dates back to 5–8 Ma, and ceased 0.03 Ma (Moore et al., 2011). At la Réunion, the onset of volcanic activity on the seafloor dates back to 5 Ma (Gillot et al., 1994) while the oldest emerged rocks are ~2 My old (McDougall, 1969). The island is composed of 2 volcanic edifices (Fig. 1), the Piton des Neiges to the North–West, inactive since about 12 ka, and the more recent (0.5 Ma) Piton de la Fournaise, about 40 km to the South–East. At the scale of our study we thus consider these three volcanoes as contemporary, signing the top outer edges of the Réunion plume.

The current paradigm is that volcanoes grow immediately above the axis of a plume head, as shown by Ceuleneer and Rabinowicz (1993) with numerical models of plumes rising in a viscous upper mantle. These models show how the lithosphere is squeezed upwards by the plume, with vertical viscous flow and thus vertical σ_1 (most compressive principal stress) at the base of the lithosphere: "*An upper zone extends to the base of the lithosphere, where the sub-vertical vein orientation will make possible rapid melt migration toward the surface*". When the buoyancy of melt bands exceeds the yield stress, dikes oriented parallel to the vertical compressive stress propagate upward. One thus expects direct transfer of melts from the plume axis to the surface. Consequently, our observation of a ca. 150–180 km offset between most recent surface volcanism and the plume axis remains enigmatic.

At La Réunion, Barruol and Fontaine (2013) proposed that Rayleigh–Taylor (RT) instabilities developing at the base of the lithosphere above the plume could explain the offset. These gravity-driven instabilities likely develop at the lithosphere–asthenosphere transition zone, when a mantle plume impacts and spreads beneath a lithospheric plate (e.g., Fleitout and Yuen, 1984). Thoraval et al. (2006) showed that for an appropriate Rayleigh number, RT instabilities can develop below a drifting plate both downstream and upstream from the plume head. Yet these instabilities reach a minimum wavelength of 200 km, and they remain of greater intensity downstream than upstream.

At Hawaii in turn, Ballmer et al. (2013) modeled the chemical evolution and fragmentation of lavas downstream from the plume. Bianco et al. (2005) studied the elastic upward flexural bulge induced by the weight of the volcanic chain. In their model, this flexural bulge decompresses the underlying asthenosphere and causes "remelting". Accordingly, Bianco et al. (2005) explain the development of arch volcanism observed at Hawaii over a circular area about 250–300 km wide around the plume axis. However the height of this flexural bulge underestimates the volumes of emitted alkaline magmas, and again the typical wavelength of this process is >200 km. Moreover arch volcanism is of secondary, alkaline-type, that differs from the primary, shield volcanism of Big Island or Loihi. Hence an explanation for upstream volcanism at both Hawaii and La Réunion is still lacking.

Mantle convection studies tend to ignore the role of elasticity because in fact it does not have a significant impact on asthenospheric flows. However, elasticity plays a fundamental role in the orientation of stresses inside the lithosphere. It is well known for example that elasticity in tectonic plates acts as a low-pass filter on geoid and topography signals on Earth (Lambeck et al., 1984; McNutt and Ménard, 1982), and several studies have evaluated an elastic thickness of the lithosphere from the flexural load exerted by volcanic seamounts (Watts and Zhong, 2000; Zhong and Watts, 2013, and references therein). We posit here that in the context of plume/lithosphere thermo-mechanical interactions under oceanic hotspots islands, elasticity also plays a central role in orienting the lithospheric trajectories of the primary melt produced by plume decompression. When a mantle plume impacts the (oceanic) lithospheric plate, like for a ruler bent upwards, horizontal compression (i.e., horizontal σ_1) develops at the base of the bent plate, closing its "pores" and thus impeding the vertical migration of melts produced right at the axis of the plume. Plume decompression-induced melts have to bypass this compressive layer and "find" bordering regions with favorable stress conditions (i.e., vertical σ_1) to reach the surface. However, lithospheres are not "just" elastic but have more complex visco-elasto-plastic rheologies. d'Acremont et al. (2003), Burov and Guillou-Frottier (2005) and others actually studied lithospheric deformation resulting from the interaction of a mantle plume with a visco-elasto-plastic lithosphere. But far-field extension is also applied in these studies, which favors rapid plate failure, and which does not apply to the setting of Hawaii nor la Réunion, where oceanic plates mainly drift rather than stretch over their corresponding plumes.

Here we first constrain (section 2) with two-dimensional numerical models of plate bending, the physical parameters that characterize the typical lengths and timing of a compressional

zone at the base of lithospheric plates. In section 3 we display numerical models at the scale of the upper mantle, in which we look precisely at the evolution of the stress field in the top ~150 km. We then analyze how melts find their way upwards and sideways to form volcanoes ~150–180 km away from the plume axis.

2. Visco-elastic plates submitted to basal loading

2.1. Analytical considerations

Hafner (1951) was amongst the first to resolve the force balance equation in a two-dimensional elastic rectangular plate, for a large variety of applied boundary stress loads. He calculated the harmonic Airy solutions of a continuous stress distribution within the plate, and showed that zones of compression and extension co-exist within consistent tectonic contexts (Appendix A). Hafner approximated the action of convective cells of wavelength $L = 2\pi/\kappa$ in the '*weak substratum below a crustal plate*' with sinusoidal stress variations applied on its base. He showed that the deepest domains inside the plate develop a tensile or a compressional state of stress, depending on the ratio of the normal ($q_n = \sigma_{yy} = -A \cdot \sin \kappa x$, where x and y designate the horizontal and vertical axes, respectively) and shear ($q_s = \sigma_{xy} = -B \cdot \cos \kappa x$) loads applied along this base. $A = 0$ refers to the development of pure drag at the bottom of the plate, whereas $B = 0$ describes vertical loading alone. The directions of the stress trajectories (Figure in Appendix A), are given by $\tan 2\beta = 1/\tan(\kappa x) \times F(y)$, where $F(y)$ is an analytical function of depth y, and β represents the angle between the outward-directed normal of the surface element and the positive x-axis (Hafner, 1951). Thus both horizontal stress directions rotate from vertical to horizontal in between uneven multiples of a quarter wavelength ($x = L/4$). The base of the plate where vertical loading q_n is maximal is under tension if $B = 2A$, or under compression if $B = A/2$.

More recently, Sleep (1992) or Schmeling and Marquart (1993) showed that the normal vertical load exerted by a plume can be evaluated from its buoyancy. A temperature contrast inside the plume head with its surroundings $\Delta T = 300\,^{\circ}\mathrm{C}$ produces a density contrast $\Delta\rho = \frac{\partial\rho}{\partial T} \cdot \Delta T \sim 30$ kg/m^3. Moreover, with a partially molten mantle about 1% lighter than melt-free mantle, the total density contrast may increase up to $\Delta\rho \sim 60$ kg/m^3. Assuming that this buoyant material occupies a vertical column $\Delta h \sim 100$ km (cf. Robinson et al., 1988), then the plume's buoyancy q_n ranges from 30 to 60 MPa. In turn, the shear stress exerted by the plume below the lithosphere depends on the viscosity of the mantle and on the velocity at which it diverges away from the plume's axis (Watson and McKenzie, 1991). Mantle zones rich in melts are associated with a viscosity as low as 10^{17} Pa s (Watson and McKenzie, 1991). In the plume head, if we assume a maximum diverging velocity of 1 m/yr distributed over a distance of 100 km, the resulting shear strain rate is $3 \cdot 10^{-13}$/s. This induces a basal shear stress q_s of the order of 0.01 MPa. Even without melting, a conventional dislocation creep power-law with strain-rates as large as 10^{-12}/s provides a viscosity of about 10^{20} Pa s at the base of a lithosphere, and a shear stress of the order of 10 MPa, e.g., barely 30% of the vertical load q_n. This information put together with the results of Hafner (1951) strongly suggests that a compressional elastic stress field can indeed develop at the base of an oceanic lithosphere above a rising plume.

The distance over which compression occurs controls the location where underlying mantle melts can rise upwards again. The width of this compression depends on the width of the plume's loading (L) with respect to the characteristic flexural width (α) of the elastic lithosphere. α verifies:

$$\alpha = \left(4EH^3/\left(\Delta\rho g \cdot 12\left(1-\nu^2\right)\right)\right)^{1/4} \quad (1)$$

where H is the elastic thickness, E is the Young modulus, $\nu = 0.25$ is Poisson's ratio, and $\Delta\rho$ is the density contrast between mantle and water. Assuming that H ranges between 50 and 90 km, E between 50 and 200 GPa and $\Delta\rho = 2300$ kg/m^3 (e.g. McNutt and Ménard, 1982), we obtain α varying between 96 km and 204 km (the mean is 150 km).

L in turn is controlled by the width over which the plume head buoyancy is significant. At about 130–170 km depth, estimates of the diameter of the Hawaiian plume conduit is ~100 km (Ribe and Christensen, 1999), and ~140 km (e.g. Zhong and Watts, 2002), respectively. Ballmer et al. (2013) also indicate a thermal buoyancy width of ca. 100 km at ~150 km depth. Consequently, the plume's loading width L is slightly smaller than the lithosphere's flexural width α, and we conclude that the width of compression depends on α.

In the next sections we study this process of plume-induced elastic flexure by means of numerical models. First, inspired by Hafner (1951), we simulate plate mechanical behavior in response to basal loads. We consider purely elastic (section 2.2) and visco-elasto-plastic plates (section 2.3). Then, we take on modeling a plume rising from 600 km depth (section 3). We use the numerical code Parovoz (Poliakov et al., 1993) described in Appendix B. This code has been benchmarked and adapted for many geodynamic purposes since the 1990's (e.g. Poliakov et al., 1993; Gerbault et al., 1998, 2012; d'Acremont et al., 2003; Burov and Guillou-Frottier, 2005).

2.2. Numerical models with an elastic plate

Our first model setup assumes a rectangular elastic plate 1200 km long and 60 km thick. Lateral borders are set free-slip, the top surface is set free. At the bottom of the plate, we choose to approximate the constant normal load $A = 50$ MPa generated by a plume over the interval $[-L/2, L/2]$, by a function $q_n = A \cdot \cos(\pi/2L)$ applied over the interval $[-L, L]$. Elsewhere along the base of the domain Archimede's restoring normal force is applied. In Fig. 2a we set $q_s = 0$ ($B = 0$). The most compressive principal stress (σ_1) is oriented horizontal in an area about 20 km thick and 200 km wide at the bottom center of the plate, coinciding with the width L of the exerted vertical load. In the upper part, tensile stresses develop (i.e., where σ_1 is oriented vertically) over a distance of 100 km from the model center, while horizontal compression re-appears about 200 km away. In between and along a vertical column at $X = \pm 150$ km, plate curvature reverses and the 2nd invariant of the stress field σ_{II} ($\sigma_{II} = (\sigma_3 - \sigma_1)/2$, where σ_1 and σ_3 are minimum and maximum principal stress components) increases from both the top and the bottom edges to reach a local maximum in the middle of the plate at 30 km depth (orange lobes in Fig. 2a).

Then we illustrate the effect of a shear stress $q_s = B \cdot \sin(kx)$ applied over one wavelength ($L = 200$ km) at the base of the plate. Figs. 2b and 2c show cases including a basal shear stress $B = 0.5A$ and $B = A$, respectively. When $B = A$ (i.e., q_s and q_n have the same amplitude), horizontal compression disappears at the bottom center of the plate, but horizontal compression still occurs about 100 km away from the center. Additional models confirm that (i) the lateral extent of horizontal compression is proportional to the loading width L (if L becomes greater than the flexural width α, Fig. 2d), and (ii) its vertical extent reduces relatively to increasing plate thickness H (Fig. 2e). Thus we conclude that the elastic horizontal compression exerted by a plume becomes negligible if the plume width is significantly narrower than the plate's elastic width α, and if the lateral shearing induced by the diverging plume head below the plate is strong.

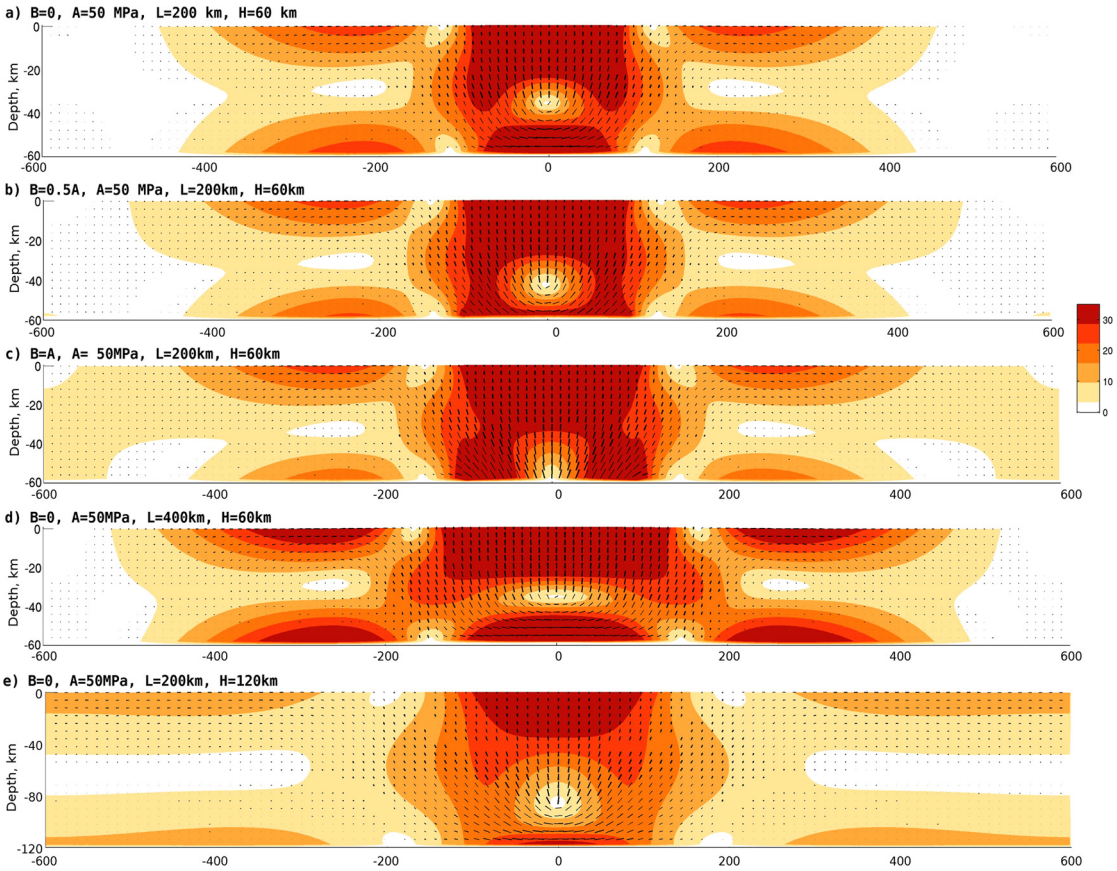

Fig. 2. Numerical models of elastic plates flexed above an applied basal load. Colored contours display the magnitude of σ_{II} (second invariant of the stress tensor) and black lines display the orientation of the most compressive principal stress (σ_1, length indicates relative intensity). a) A reference case with only vertical loading $qn = A \cdot \cos kx$, with $A = 50$ MPa and over a horizontal width $L = 2\pi/k = 200$ km. Plate thickness is 60 km. The horizontal orientation of σ_1 indicates compression at the bottom center. b) Same as a) with an additional shear stress applied at the base of the plate $q_s = B \cdot \sin kx$, with $B = 0.5A$. c) Same as a) with additional shear stress q_s and $B = A$. Note that, at the base of the plate center σ_1 is now oriented vertical, while σ_1 remains horizontal at some distance away around $x = L/2$. d) Same as a) with a broader applied load, $L = 400$ km. e) Same as a) but with a plate thickness $H = 120$ km. (For interpretation of the references to color in this figure, the reader is referred to the web version of this article.)

2.3. Visco-elastic plate models

Here we define the same setup as above but assume viscoelastic Maxwell plates:

$$\dot{\varepsilon} = \dot{\sigma}/2G + \sigma/\mu \tag{2}$$

written with the second invariants of the stress σ and strain-rate $\dot{\varepsilon}$, viscosity μ and shear modulus G ($G = 2E/5$, assuming plane-strain and a Poisson's ratio $\nu = 0.25$, cf. Appendix B). Tested viscosities μ range from 10^{23} to 10^{25} Pa s, and elastic shear moduli from $G = 10$ to 80 GPa. Fig. 3a displays the stress field evolution for $\mu = 10^{24}$ Pa s, $G = 50$ GPa, and zero applied tangential shear stress ($B = 0$). Horizontal compression builds up immediately at the bottom of the plate, and vanishes within about 5 My. After 6 My, σ_1 has completely rotated to vertical. This indicates a dominant viscous response to the applied vertical load from below, which squeezes the intermediate viscous domain, as shown by previous studies (e.g. Ceuleneer and Rabinowicz, 1993).

Fig. 3b presents a simulation with a temperature-dependent rheology. We assume a linear increase of temperature up to 700 °C or 900 °C at the base of the plate. Effective viscosity is calculated with a common dislocation-creep law for dry olivine (Chopra and Paterson, 1984, Table B.1). As a result, instantaneous elastic compression affects the plate's bottom 30 km. With time the warmest deep domains relax viscously and compression vanishes. The domain above has viscosities greater than 10^{25} Pa s, so that elastic horizontal stresses are maintained as long as the basal load is maintained.

It is important to understand how long horizontal compression is maintained prior to viscous relaxation (e.g. the Deborah number illustrated by Poliakov et al., 1993), and consequently how long it prevents melts from climbing directly up to the surface above the plume head. Fig. 3c displays the temporal evolution of the maximum of σ_{II} within the bottom half of the plate. While an elastic plate maintains its stress upon equilibration (red curve), visco-elastic plates relax part of this stress at their Maxwell rate ($\tau_r = \mu/G$), and elastic flexural stresses diminish by half within 0.3 My for a plate viscosity $\mu = 10^{23}$ Pa s, within 3 My for $\mu = 10^{24}$ Pa s, and within 30 My when $\mu = 10^{25}$ Pa s. The elastic response of the Maxwell body is progressively taken up by its viscous response. In the case with temperature-dependent viscosity, half of the elastic flexural stress relaxes after 20 My when the basal temperature is set at 900 °C, and it relaxes even slower when the basal temperature is set at 700 °C. Fig. 3c indicates that for horizontal compression to last more than 5 My, the viscosity of the plate between 500 °C to 900 °C must exceed 5×10^{24} Pa s.

When a diverging basal shear stress q_s ($B = 0.5A$) is applied in addition to vertical loading q_n (Fig. 3d), the maximum instantaneous elastic stress is reduced because the initial vertical load is partly balanced by basal shear, whereas the asymptotic viscous stress increases since it includes this applied shearing. Finally, if the elastic modulus of the plate is increased ($G = 80$ GPa, dotted curves in Fig. 3d), the instantaneous σ_{II} increases, but its asymptotic value is reached earlier (because of the smaller relaxation time $\tau_r = \mu/G$). Finally, a plate with temperature-dependent vis-

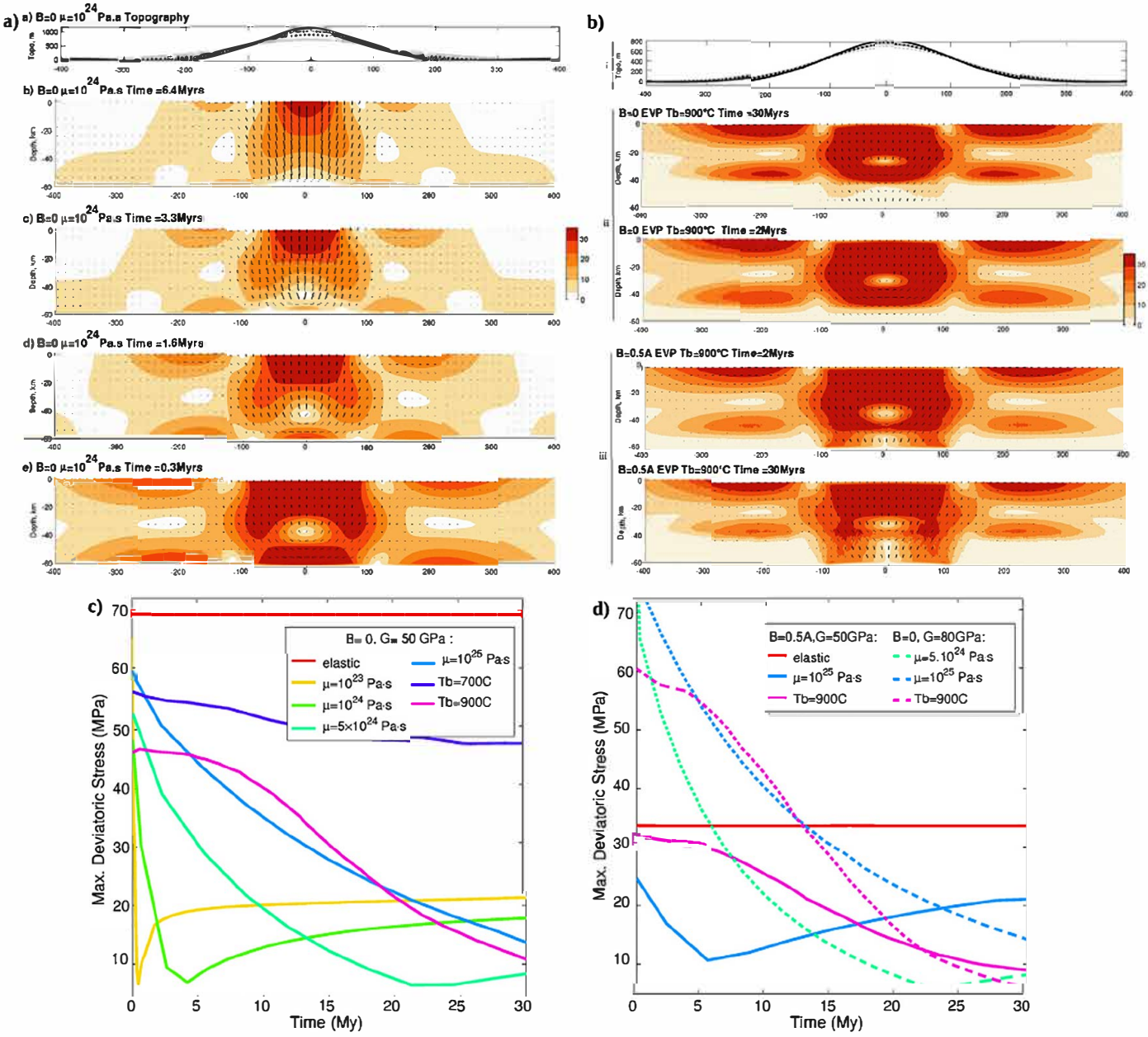

Fig. 3. Stress distribution in visco-elasto-plastic plates submitted to a vertical basal load $q_n = A\cos(kx)$. a) Stress field in a plate with viscosity $\mu = 10^{24}$ Pas, $G = 50$ GPa. Top panel displays the growing topography for time-steps 0.6, 1.5, 3 and 6 My. b) Stress field and topography for two cases ($B = 0$ and $B = 0.5A$) with temperature-dependent power-law creep rheology and a top-to-bottom linear temperature gradient up to $Tb = 900\,°C$. Top panel displays the topography for both cases, panel (ii) displays 2 timesteps after 2 and 30 My for case with $B = 0$, panel (iii) displays these time-steps for $B = 0.5A$. Same legend as in Fig. 2; c) and d) Temporal evolution of the maximal value of σ_{II} at the bottom of the modeled plates. Each curve corresponds to a different rheology, illustrating how fast the amplitude of horizontal compression decreases with decreasing plate viscosity. Cases with a temperature dependent viscosity (fuchsia lines) show a decrease intermediate between the pure elastic response and a visco-elastic plate of viscosity between $5 \cdot 10^{24}$ and 10^{25} Pa s (in green and blue). d) Displays cases with a shear stress at the base ($B = 0.5A$, plain curves), and cases with a greater shear modulus (G, dotted curves). (For interpretation of the references to color in this figure legend, the reader is referred to the web version of this article.)

cosity behaves always stiffer than a plate of constant viscosity 10^{25} Pa s for at least the first 10 My.

3. Models of plume-lithosphere interaction

We implement another setup in a domain 2400 km wide and 600 km deep. We define an initial background temperature that satisfies the conductive solution in the top 250 km of the domain, with a conventional *erf* function depending on the age of the oceanic lithosphere. Deeper than 250 km, the temperature is adiabatic with a gradient 0.3 °C/km. At the bottom of our modeled domain in an area of diameter 100 km, we impose an excess temperature of 300 °C and a density contrast of 30 kg/m^3 (similar to Burov and Guillou-Frottier, 2005). This anomaly rises and impacts the lithosphere within about 8 My, and from then on we study its interaction with the lithosphere.

3.1. A reference model (M1)

Model M1 assumes a plate 70 My old (Figs. 4, 5). We count Time (Tr, in My) relative to the time when the isotherm 1600 °C roughly reaches 170 km depth (*domain A*, Fig. 4a). This temperature is close to but lower than the dry solidus of the mantle (Walter, 1998; Herzberg and Asimow, 2015). It is inferred that our modeled temperature field corresponds to a reasonable case of hydrated plume (Bercovici and Karato, 2003).

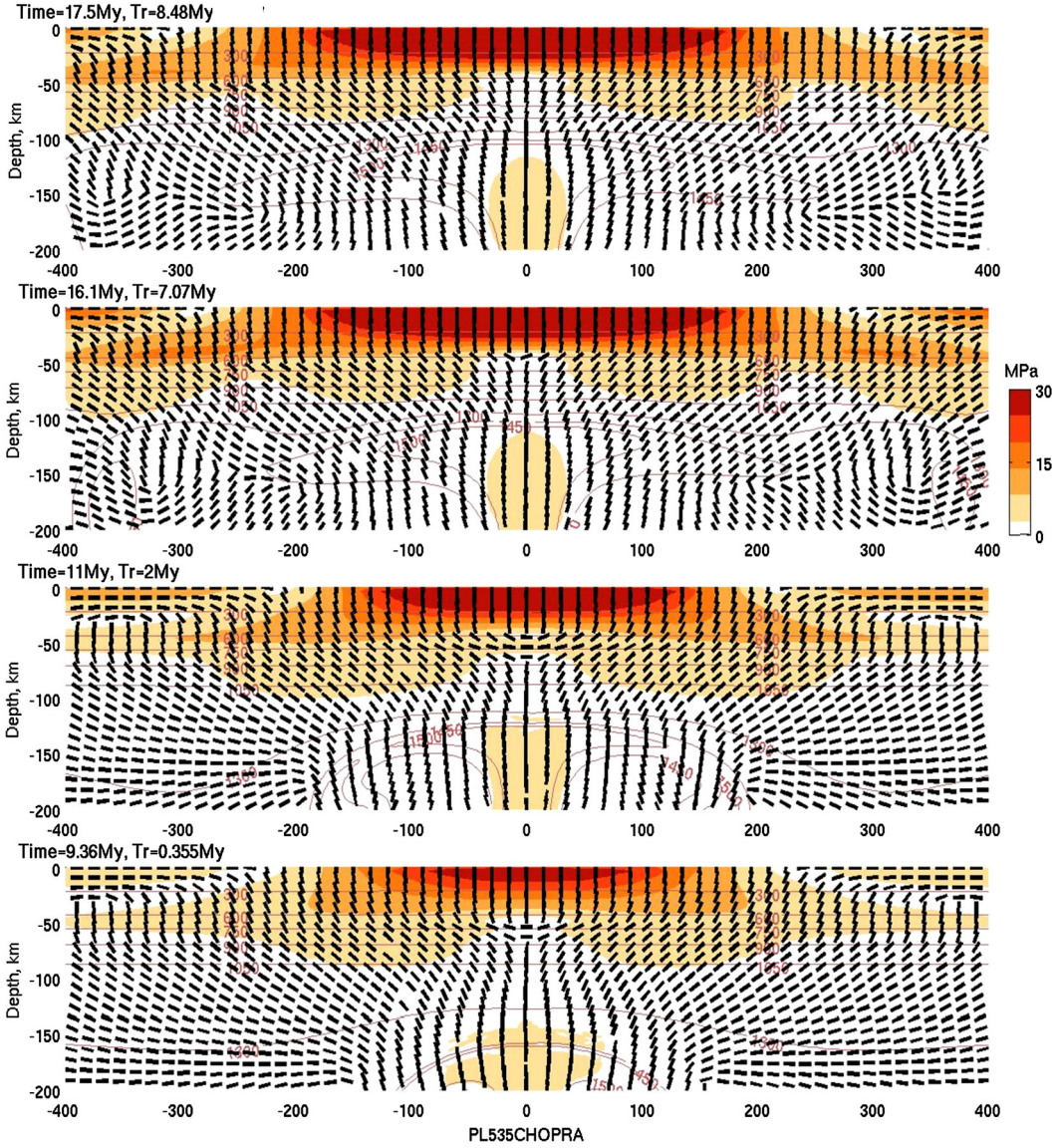

Fig. 4. Numerical model of a plume rising below a visco-elastic plate. Model M1 with plate of 70 My and $\Delta T = 300\,^{\circ}\mathrm{C}$, power-law creep by Chopra and Paterson (1984) and $G = 80$ GPa. Four time-steps during plume expansion: orange to brown contours display the amplitude of the second stress invariant (σ_{II}) and black lines display the orientation of σ_1 (irrespective of its amplitude). Horizontal compression develops at the center of the model at ca. 50–70 km depth, and it vanishes within about 7.5 My. (For interpretation of the references to color in this figure legend, the reader is referred to the web version of this article.)

From $Tr = 0$ My onwards, the rising plume generates horizontal compression in between its head and the base of the lithosphere, thus producing the source load for lithospheric flexure. Fig. 4 displays four time-steps, while Fig. 5 displays details for specific time $Tr = +2$ My. Horizontal compression develops in the depth range 50–70 km (*domain B*, Fig. 5) in a domain where the first invariant – the mean value of the principal stresses (the third of the trace of the stress tensor) minus the lithostatic pressure ($\rho g y$, where y is depth) – is negative (positive relative pressure). This domain extends down to ~150 km depth (encircling the heart of the plume, where temperature reaches ~1500 °C) and covers a distance exceeding 200 km from the plume axis. In domain B bounded by isotherms 600 °C and 900 °C, viscosity varies by at least 5 orders of magnitude (Fig. 5c) and "elastic compression" occurs (the first invariant is negative and σ_1 is horizontal). There, the relatively small amount of horizontal compression (~20 MPa) at the plate center (i.e. $|X| < 100$ km), and the presence of shear stress further away at $|X| > 100$ km implies the occurrence of shearing (q_s) at the base of this lithosphere, as evidenced by the models of section 2.3. After $Tr = 7.5$ My (Fig. 5d), stresses at the center of domain B rotate to vertical, in a similar way to the models of section 2.3.

Horizontal compression at the base of the lithosphere persists in competition with (i) horizontal divergent shearing exerted by the plume, and (ii) thermal erosion that weakens the deepest resistant levels of the lithosphere. As discussed previously, horizontal shearing at the base of the lithosphere depends on sub-lithospheric viscosity. If viscosity is too high there, then the diverging plume flow occurs at high shear stress that generates extension within the oceanic plate (see models in section 2 with a large B). The presence of melts wetting the mantle solid grains (Kelemen et al., 1997) would tend to reduce the plume's bulk viscosity and shear stress amplitude, helping horizontal compression. On the other hand, thermal erosion of a lithosphere by a plume only becomes significant after a time-scale of the order of 10 My (Monnereau et al., 1993; Ribe and Christensen, 1999), which exceeds the timing of renewal of the drifting plate over the plume head.

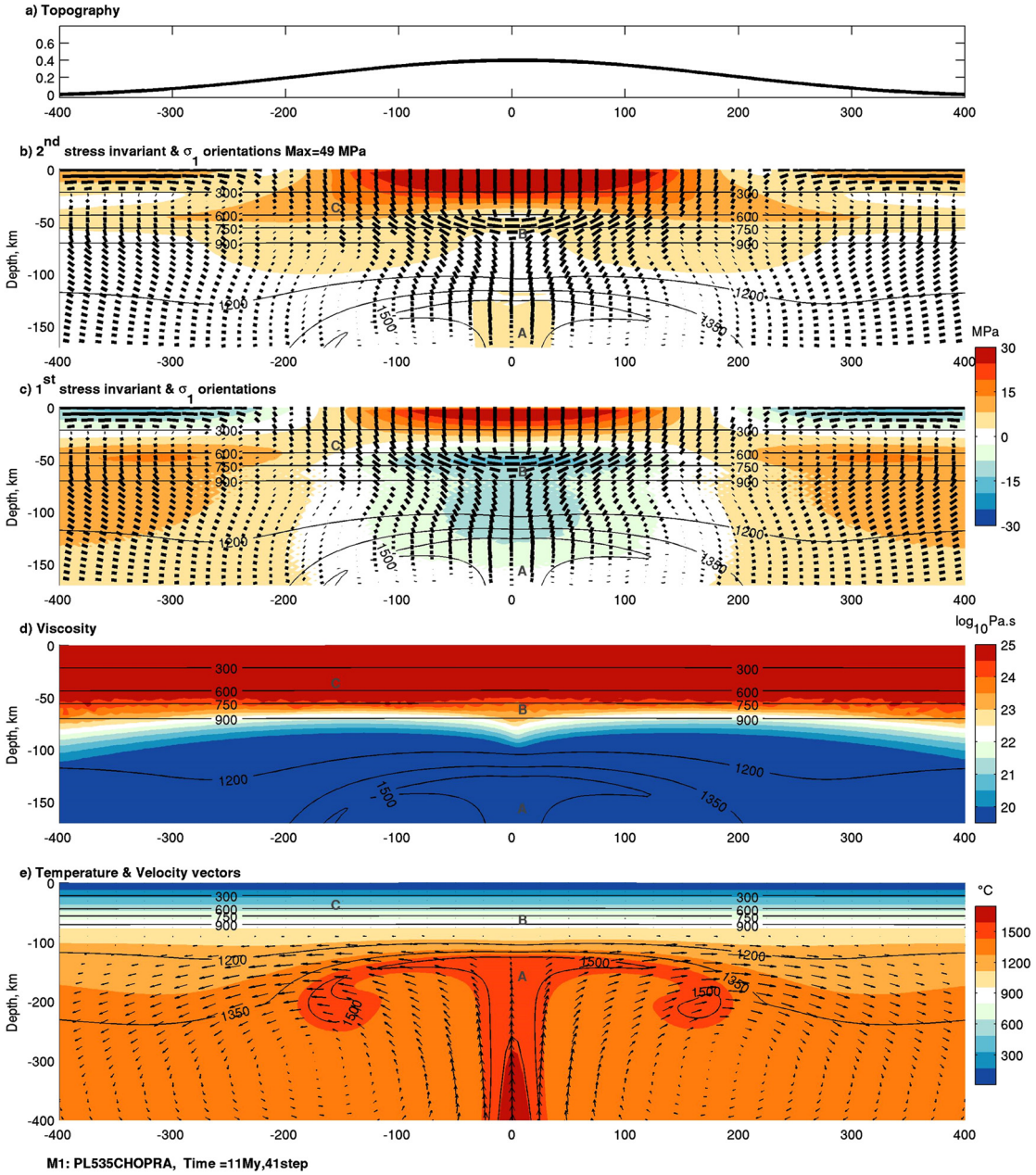

Fig. 5. Details of model M1 with a plate 70 My old and plume $\Delta T = 300\,^{\circ}\mathrm{C}$, after time $Tr = 2$ My (Fig. 4b): a) shows surface topography. (b) and (c) display the 2nd stress invariant (σ_{II}) and the 1st stress invariant (minus lithostatic pressure) of the stress tensor, respectively, superimposed with the orientations of σ_1. (d) displays the viscosity down to 180 km depth, and bottom panel (e) displays the temperature field down to 400 km depth, with temperature isocontours (°C, black lines). Upon impact of the plume head (domain A) on the base of the lithosphere, horizontal compression develops at ∼65 km depth in domain B. Mantle derived melts from domain A are inferred to be deviated laterally over a distance of ∼170 km, prior to ascending further into domain C, where they pond again due to reversing plate curvature (where σ_{II} reaches a local maximum along that vertical column). (For interpretation of the references to color in this figure, the reader is referred to the web version of this article.)

3.2. *Influence of rheological parameters*

The temperature-dependent visco-elastic rheology of the lithosphere controls the preservation of horizontal compression in domain B via its Maxwell relaxation time. Between 600 and 1000 °C, viscosity decreases from ca. 10^{26} to 10^{23} Pa s (Fig. 5). Parametric tests help us gain insight on dominant trends regarding this relaxation.

Effect of lithospheric thermal age If we consider a lithosphere of age 100 My, compression develops from 73 km depth down to ca. 40 km depth over a characteristic distance from the plume head ∼190 km, and lasts for 10 My (model M2 in Table 1, Figs. 6, 7). For a young lithosphere 30 My old, compressional elastic bending initiates at depth ∼45 km (Fig. 7) and lasts ∼5 My, after which σ_1 turns vertical above the plume head. Fig. 6 illustrates an alternative case (M7) in which the lithosphere is 100 My old and the plume is warm (thermal anomaly $\Delta T = 400\,^{\circ}\mathrm{C}$): isotherms 1600 °C reach ∼130 km depth (exceeding the solidus of a dry mantle) within about 9 My ($Tr = 2.5$ My). Horizontal compression initiates deeper (75 km), and persists longer (8 My) than in our reference model M1 (cf. Table 1). This indicates that plume-volcanism offset persists best in mature oceanic lithospheres. Since the Réunion and Hawaiian lithospheres have thermal ages of 70 and 80 My respectively, we expect that the characteristic time duration of flexural compression is of the order of 5 My there (Fig. 8).

Table 1
Plume model tests according to Plate Age, elastic shear modulus G, rheological law Q^*, and plume basal temperature anomaly Tp. $Q^* = 535$ refers to the power-law creep parameters proposed for dry dunite by Chopra and Paterson (1984), and $Q^* = 520$ refers to the law used by Burov and Guillou-Frottier (2005) (see Appendix B for details). Peierls mechanism in M8 is accounted for when $T < 800\,^{\circ}C$. The resulting time duration of horizontal compression at the base of the lithosphere, and predicted offset of plume and surface volcanism are depicted in the two last columns.

	Plate age (My)	Shear modulus G (GPa)	Rheology Q^*	Plume anomaly T_p (°C)	Compression time (My)	Flexural width (km)
M1	70	80	535	300	7.5	170
M2	100	80	535	300	10	190
M3	30	80	535	300	5.5	130
M4	70	50	535	300	4.5	150
M5	70	80	520	300	7	165
M6	70	80	535	400	7.5	175
M7	100	80	535	400	8	190
M8	70	80	Peierls	300	7.5	170

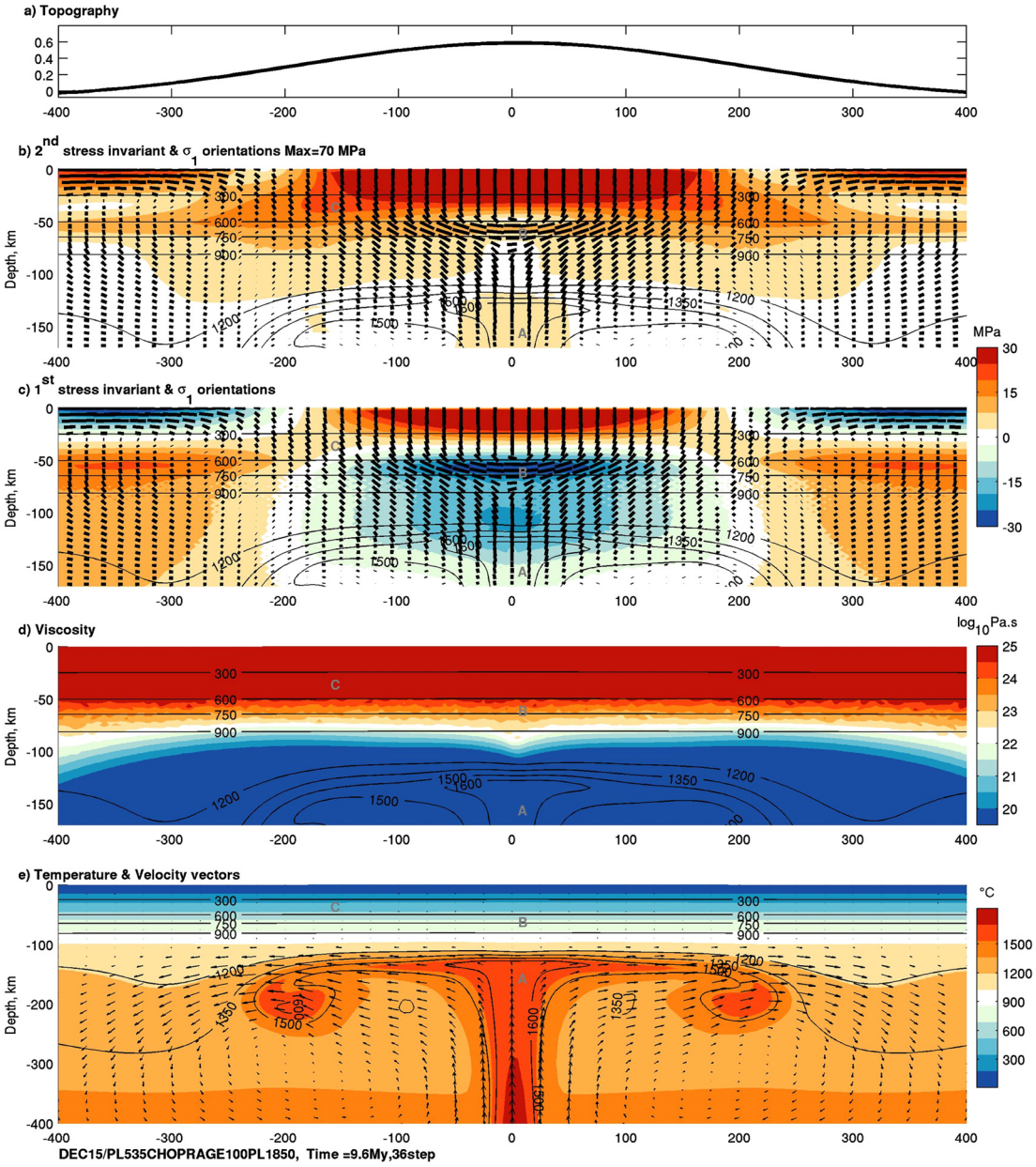

Fig. 6. Model M9 with a plate age of 100 My and a plume initial temperature with $\Delta T = 400\,^{\circ}C$ after time $Tr \sim 2.5$ My. Legends as in Fig. 5. Note the warmer isotherms in the plume domain and the cooler isotherms in the lithosphere above, generating a deeper rotation of the compressive stress compared to M1 (Fig. 5). (For interpretation of the references to color in this figure, the reader is referred to the web version of this article.)

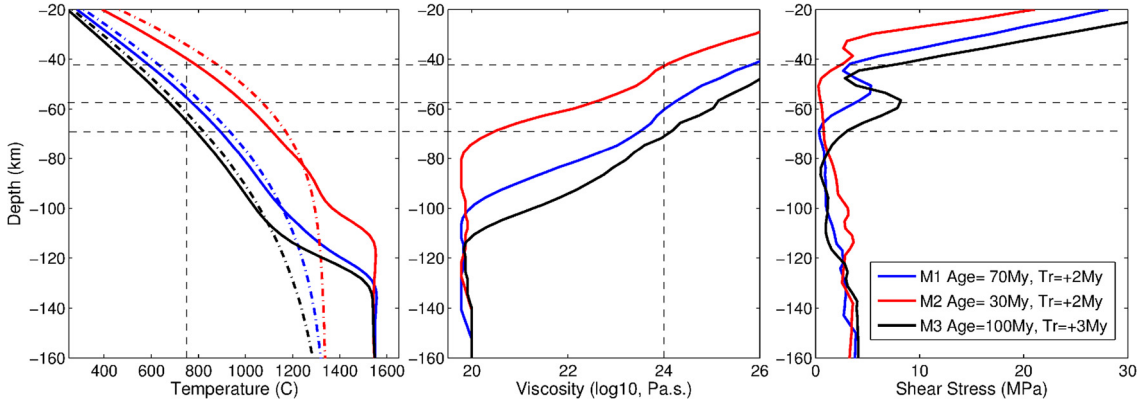

Fig. 7. Vertical profiles at model centers for 3 models with variable lithospheric age (30–70–100 My) at similar times $Tr \sim 3$ My. From left to right, temperature, viscosity, and (σ_{II}) are plotted. Dotted horizontal lines indicate approximate depth from where horizontal compression develops, around $T = 750\,^{\circ}$C in all three cases.

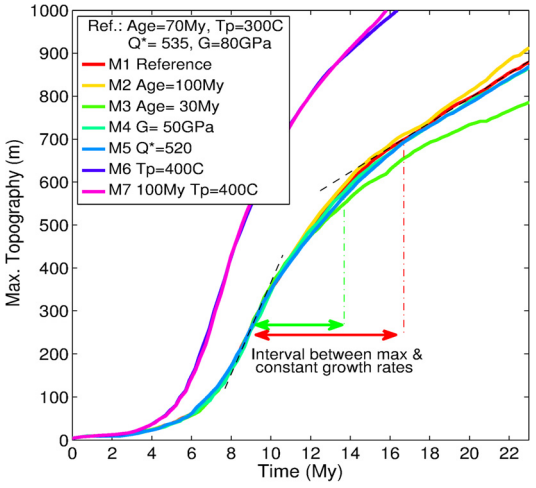

Fig. 8. Topography with time for models M1 through M7 (cf. Table 1). Double-arrows indicate the approximate time interval during which flexural compression develops for the reference model M1 (in red) and for model M3 (in green), coinciding with the inflexion points of topographic growth. (For interpretation of the references to color in this figure legend, the reader is referred to the web version of this article.)

Effect of shear modulus Model M1 (Figs. 4–5) assumes a shear modulus $G = 80$ GPa (Bass, 1995). Many modeling studies assume $G = 30$–50 GPa or less (Watts and Zhong, 2000). While this value may be acceptable for continental mantle lithosphere or damaged lithospheres in general, it is likely an under-estimation for 'intact' oceanic lithospheres. Different estimates based on experimental rock mechanics (e.g., Bass, 1995; Stixrude and Lithgow-Bertelloni, 2005), and modeling of petrological assemblages for oceanic lithosphere (e.g., Afonso et al., 2008) provide values of G close to 80 GPa. In our models when decreasing G to 50 GPa, the timing of compression significantly decreases down to 4.5 My (model M4, Table 1), despite the relaxation time increases. This apparent paradox results from smaller amplitude of flexural elastic stresses to be relaxed by viscous flow (which thus occurs faster), as already shown in section 2.3.

Effect of viscosity laws The model M1 uses a relatively strong power-law, proposed by Chopra and Paterson (1984) for dehydrated dunite, with $Q = 535$ kJ/mol, $n = 3.5$ and $A = 2.9 \times 10^4$ MPa^{-n}/s. If we adopt a slightly softer power law (model M5 in Table 1) used by Burov and Guillou-Frottier (2005) and others ($Q = 520$ kJ/mol, $A = 10^4$ MPa^{-n}/s, $n = 3$), then the duration of horizontal compression is reduced by up to 1 My. The depth of maximum compression is only reduced by a couple of kilometers, so that the corresponding flexural distance to the plume center reduces by about 10 km. Low-temperature plasticity creep (Peierls mechanism prescribed for $T < 800\,^{\circ}$C as in Zhong and Watts, 2013) does not significantly affect the timing nor extent of horizontal compression (model M8, Table 1).

Both results with lower shear modulus and 'softer' viscous creep parameters indicate that plume-volcanism offset is not expected to be a typical feature in continents or damaged mantle lithosphere.

3.3. Considerations on topography

In comparing the timing of compressional elastic bending to topographic evolution, the onset of horizontal compression at ca. $Tr = 0$ My occurs approximately when the topography increase starts to slow down after rapid plume rise from 600 km depth (Fig. 8). This is because the plume slows down as it encounters increasingly viscous material approaching the surface. From that moment on, the plate's mechanical response progressively evolves from purely elastic to dominantly viscous. The end of elastic compression in turn, coincides with a stabilization of topographic growth at ca. $Tr = +7.7$ My (Fig. 8). From that moment on, the modeled constant increase in topography is consistent with the idea of stable viscous deformation resulting from a constant plume load.

Note from Fig. 8 that a maximum topography of 1 km is reached about 10 My after the arrival of the plume at the base of the lithosphere. The associated amplitude of this swell is about 1000 km, which is consistent with estimates for la Réunion (Bonneville et al., 1988) and Hawaii (Ribe and Christensen, 1999).

3.4. Plate drift versus timing of visco-elastic flexural compression

Contact with the lithosphere occurs at a distance upstream to the plume axis that approximately equals $\max(L/2, \alpha/2)$ (L: plume loading width, and α: lithosphere flexural parameter). Consequently, at the plume axis, the plume load acts during a time $\max(L/2, \alpha/2)/Vp$, where Vp is the plate drift velocity. This reasoning only applies upstream of the plume, since the rheological and magmatic evolution of the lithosphere downstream is obviously more complex (e.g., Ribe and Christensen, 1999; Ballmer et al., 2013). The stress field in the lithosphere at time $Tr = \max(L/2, \alpha/2)/Vp$, is 3 My for la Réunion ($Vp = 2.5$ cm/yr), and 1.3 My for Hawaii ($Vp = 7.5$ cm/yr). At these model times horizontal compression is still maintained over ca. 150 km from the plume axis (cf. Table 1). This shows that the offset of primary volcanism upstream from the plume head is actually a persistent feature.

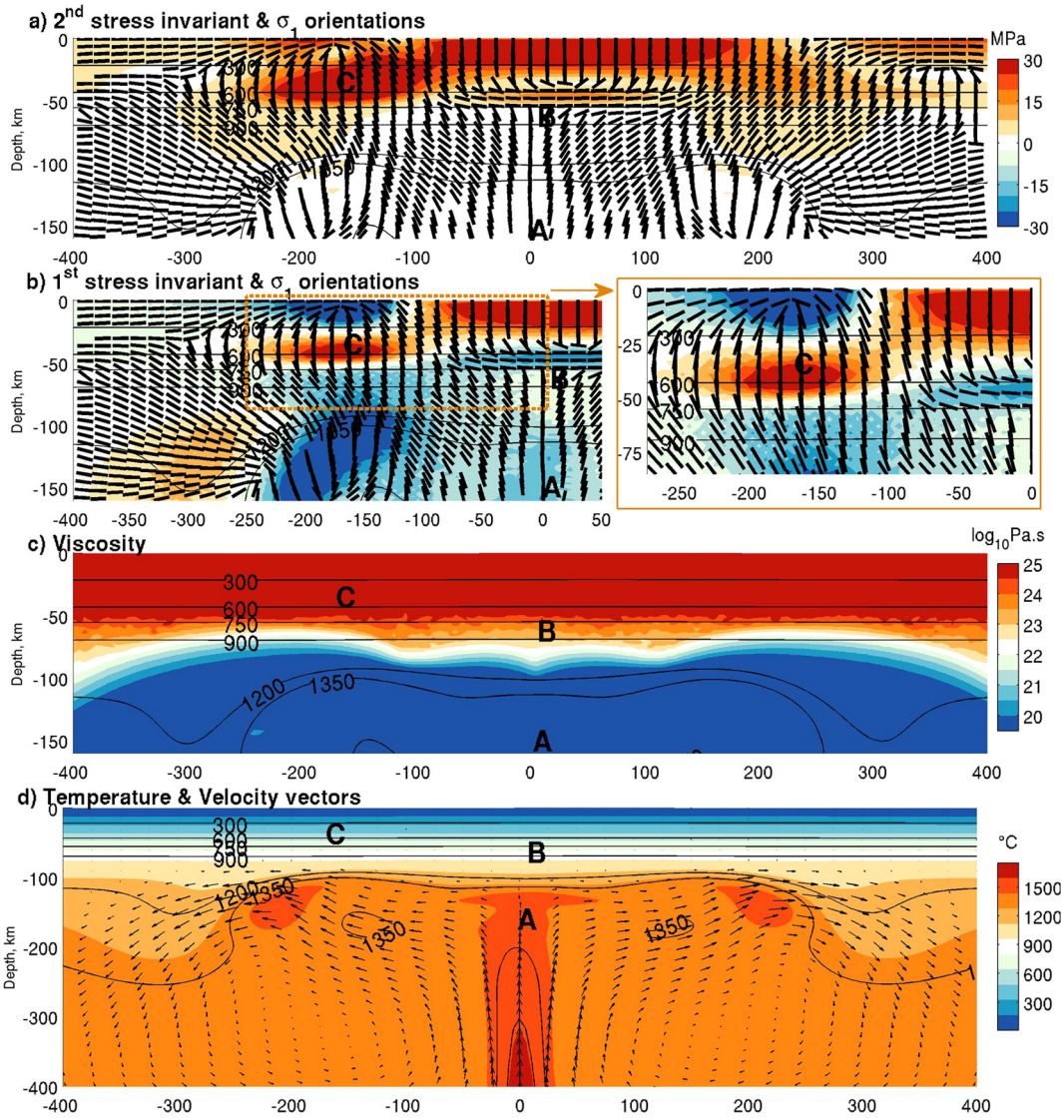

Fig. 9. Model with an additional normal gaussian load applied on the top surface, which progressively increases to a maximum of 100 MPa centered at $X = -160$ km (upstream from the plume head where we predict the onset of surface volcanism). Legend as in Fig. 5, with additional inlet displaying a zoom around the area of the volcanic edifice. This offset load increases the magnitudes of σ_1, and tension now exerted in domain C tends to suck up the melts coming from below domain B. (For interpretation of the references to color in this figure, the reader is referred to the web version of this article.)

3.5. The additional effect of loading by a volcanic edifice

Downward flexure exerted from above due to island loading is well known to induce horizontal tension at depth, which thus superimposes on the compressional stress field induced by plume loading. Lithospheric stress orientations, and by extension magma trajectories, must therefore be considered as they evolve together with the progressive building of volcanic islands.

In Fig. 9 we show the effect of the downward load exerted by a volcanic island located upstream from the plume (e.g., Big Island, La Réunion, Mauritius). We consider a Gaussian normal load applied on the top surface centered at $X = -170$ km, of characteristic width 30 km and amplitude 100 MPa ($\rho gh \sim 3000 \times 10 \times 3$ km). It starts to develop at relative model time $Tr = 0$ My. The generated downward flexure produces a reversed orientation of the most compressive stress compared to that produced by the upward load exerted by the plume head. Both these loads being offset by a distance of ~170 km, the load from above has the effect of focalizing and enhancing horizontal extension right inside domain C (tension occurs now from ~30 km depth downwards), as well as enhancing horizontal compression right above the plume head in domain B (at $X \sim 0$).

The situation in Hawaii is more complex. In Hawaii, primary shield-type volcanism occurs not only upstream (i.e., Big Island) but all the way "up" to the inferred axis of the plume (e.g., Maui) in the last My (Ballmer et al., 2013). Actually the Hawaiian volcanic chain can be seen to lie over a 100 km-wide ~North/South "lithospheric slot", that extends 400 km along the direction of plate motion. This slot consists in damaged lithosphere resulting from both, a ~North–South relative tensile stress throughout the Pacific lithosphere, and from repeated dyke injections, magma ascent and volcanic edifice loading (e.g., Sandwell and Fialko, 2004, and references therein, Stuart et al., 2007). In this slot the strength of the lithosphere is significantly reduced as shown by Zhong and Watts (2013), who showed that weak visco-elastic properties (elastic thickness <30 km, low friction coefficient and low creep activation energies) are required to fit the geometry of the deflected Moho. Consequently we visualize that the rigidity of the lithosphere inside this slot is significantly smaller than beyond the ~100 km wide volcanic chain (indicating an anisotropic elastic thickness). Since the volcanic loading coincides with the slot's orientation,

the resulting elastic response is damped in that direction. However, this "weak slot" has not yet propagated much upstream from the plume head, so that there, flexure of a 70 km thick competent lithosphere still applies. The edge of this weak slot might actually be delimited by the observed secondary alkaline volcanism, which extends from the plume axis downstream (e.g. from Maui, and 200 km downstream from Big Island, Bianco et al., 2005). This secondary volcanism might actually witness the propagation of this slot (or crack, Stuart et al., 2007) and the accumulation of magma at mid-lithospheric depth, producing a mechanically decoupled lithosphere, like in continents with bimodal upper and lower competent layers (Burov and Diament, 1995). Actually in order to fully model the Hawaiian case, one should introduce in 3-dimensional models such anisotropic properties (and brittle plastic behavior) due to the propagation of this slot (which actually acts as a propagating mega-crack, Stuart et al., 2007; Rubin, 1995). One should then also track the timing of emplacement and growth of volcanic edifices, together with the far-field conditions that accompany plate drift. Meanwhile to a first order we have the feeling that our model of horizontal compression exerted by the plume head also applies to Hawaii, and explains the onset of most recent volcanism upstream from the swell.

4. Discussion, melt propagation and plate thickness

4.1. A conceptual model for magma storage and migration

Crosschecks between various observed melt impregnations in ophiolites, rock experimentation (Schmocker et al., 2003), analog modeling (e.g., Watanabe et al., 2002; Ménand et al., 2010), and models of melt/plastic mantle dynamical interactions (Rabinowicz et al., 2010) confirm that the orientation of σ_1 mainly governs melt-mantle separation. Melt layers develop oriented parallel to σ_1, and are composed of series of melt rich impregnations with a rugby-balloon shape that are hydro-dynamically connected one with the other (Rabinowicz and Ceuleneer, 2005). The thickness of these melt rich layers is $2 \cdot l_c$, where l_c represents the compaction length (Bercovici et al., 2001). Rabinowicz and Ceuleneer (2005) showed that typical values of l_c for the molten upper mantle are ca. 400–500 m, e.g., the melt layer is sub-kilometric.

Analytical and numerical considerations on the effective pressure (the difference between the fluid and solid pressures) at the top of melt rich spheroids show that it equals $\delta\rho \times g \times l_c$ ($\delta\rho$ is the mantle and liquid density contrast, ~500 kg/m^3). With a tilted σ_1, a melt-rich layer becomes tilted too, and melts circulate towards the one located just above it (Rabinowicz and Ceuleneer, 2005). Besides, because of shear deformation, individual rugby balloons stretch along the σ_1 orientation and become contiguous one with the other (Rabinowicz et al., 2010). It results that the effective pressure builds up at the top of the connected tilted melt-rich column to a maximum $\delta\rho \times g \times l$, where l represents the integrated height of this connected column.

In our models, melt rich horizons lean on the ~1200 °C interface, at the lithosphere/partially molten mantle interface. Considering our modeled stress field, we thus expect melts to migrate sideways from the plume head ($X \sim 170$ km) following the curved path formed by σ_1 orientations: from a quite vertical dip at the borders of our modeled plume at ~100 km depth (isotherm ~1200 °C), σ_1 trajectories curve outwards upwards, bypassing domain B under compression up to ~50 km depth (isotherm ~600 °C), so that we can deduce that melt rich horizons together with the stretched set of rugby balloons form a connected impregnated system over a height of ~50 km. This implies that the effective pressure build-up at the lithosphere/partially molten interface can reach 250 MPa. Such a value is high enough to trigger hydraulic fracturing of the lithosphere (Rubin, 1995; Burov and Guillou-Frottier, 2005; Gerbault et al., 2012). Dykes form that transport a great amount of the melt contained in the melt-rich sub-vertical impregnations. In the top ~50 km along a column at $X \sim -170$ km, σ_1 actually adopts a nearly vertical orientation up to the surface. We see from Fig. 5 that from ca. 70 km depth upwards to ca. 35 km depth, both the 1st and the 2nd stress invariant increase (red tones in Fig. 5c–d). Melts propagate upwards pumped by this deviatoric stress. But melts also loose part of their driving buoyancy on their way (frictional heat and material loss), and at ~35 km depth, not only do they become less buoyant, but the ambient driving deviatoric stress also starts to diminish upwards (plate curvature reverses). Therefore these melts pond in domain C and likely form a reservoir.

Joint inversion of receiver functions and surface wave dispersion data imaged a magma reservoir at 30–35 km below la Réunion island (Fontaine et al., 2015), and a conceptual model for magma transport from this depth to the surface based on petrological, geological and micro-seismic data was proposed (Michon et al., 2015). This reservoir could result from such propagation and trapping mechanisms between domains B and C. Further differentiation within this melt horizon may lower densities until a new generation of magmas acquires sufficient buoyancy to resume ascension, so that dykes propagate further up to the crust-lithosphere interface where density contrast becomes neutral again. Such a paleo-zone of storage, termed lithospheric underplating, is also imaged by seismic tomography below La Réunion (Gallart Muset et al., 1999; Fontaine et al., 2015) at 10–15 km depth. Lithospheric underplating is also evidenced below Mauritius at similar depths. Mauritius Island is located on the Eastern edge of the Réunion plume axis, and its activity dates back to less than 30 ka (Moore et al., 2011). Thus with a nearly contemporaneous activity, the Mauritius, the Piton de la Fournaise and Piton des Neiges volcanoes form a consistent half-circular geometry. Such a half-circular geometry of laterally extruded melts sideways around the plume head is coherent with our description of 3-D flexural bulging of the lithosphere up-flow from the plume head.

The construction of the island at the top of the emerging dykes loci drastically modifies the stress field around point C (Fig. 9). Actually, the resulting increase in horizontal tensile stress at 35 km depth implies that melt ponding becomes impossible there. Consequently they resume their ascension. But at about 15 km depth, the stress field becomes compressive again (we enter the domain of elastic compression induced by the volcanic edifice), reaching ~100 MPa or more. This may eventually again, favor melt ponding close to this crust-mantle interface. From 15 km depth to the surface in turn, we expect further complex tectono-magmatic damaging as lithospheric pre-structuration and Mohr–Coulomb brittle behavior enter into play, and which are recognized to operate at La Réunion (Michon et al., 2015).

At Hawaii as well, Wech and Thelen (2015) interpreted a deep seismic cluster, at ~40 km depth and located offshore South–West of Kilauea volcano, as an evidence of a persistent magma source/reservoir. According to Wech and Thelen (2015), this reservoir would receive melts from the plume and feed laterally shallower magma chambers beneath the axis of Kilauea. This magma reservoir at a depth roughly similar to the one below La Réunion could also result from the melt propagation and trapping mechanisms described above.

4.2. Comments on effective elastic thickness

In model M1 at $Tr = 0$ My (Fig. 4a), compression initiates at a maximum depth $H = 70$ km at a temperature of 900 °C, immediately above the plume head. At $Tr = 7.5$ My (Fig. 4c), the depth of compression is shallower at ca. 45 km, where temperature is ~600 °C. The ~650 °C isotherm is often associated with

the elastic thickness of lithospheres at fracture zones and subduction zones, while the 400 °C isotherm is used instead in estimates of elastic thicknesses below seamounts (Burov and Diament, 1995). In our models this 400 °C isotherm actually occurs at about 35 km depth, which happens to be consistent with the long-term elastic thickness estimate for La Réunion island (32 km, Calmant et al., 1990, measured thus ∼170 km South–East from the plume). This depth is also close to that estimated across Hawaii's main island (25–30 km, Zhong and Watts, 2013). These differences in the amplitude of the elastic thickness between la Réunion and Hawaii may be attributed to a mechanically weaker lithosphere at Hawaii than in La Réunion, because of brittle failure, Peierls plasticity, magma ascent, repeated intrusions and progressive loading by the volcanic edifice (e.g., McNutt and Ménard, 1982; Stuart et al., 2007; Zhong and Watts, 2013; Lyakhovsky and Ben-Zion, 2014, cf. also discussion section 3.5).

In addition, a consequence to edifice loading is that the domain in tension at depth greater than 30 km can possibly host primary melts from the plume. This magmatic storage would tend to confine the elastic response of the lithosphere to the top 30 km. It will also influence the visco-elastic properties of the lithosphere below 30 km, in the "reference" 400–650 °C depth range, by possibly increasing these mean temperatures and reducing the lithosphere's bulk viscosity. However this effect might not immediately influence the visco-elastic response of the lithosphere to the buoyant plume head, since 1) it initiates ∼150 km upstream from this plume head as the edifice builds up, and 2) melt accumulation and modification of the lithosphere's bulk viscosity takes time (processes to be looked at to improve the present models).

5. Conclusion

We show that a ∼150 km offset of surface volcanism upstream from the plume axis as inferred by seismic tomography at la Réunion island can be explained by transient visco-elastic plate flexure. Elastic flexure above the plume head produces horizontal compression in the base of the lithosphere in the 600–900 °C range, that prevents incoming buoyant mantle melts from rising immediately upwards through the lithosphere. Consequently these melts can only be expelled where compression vanishes laterally, at the plate's flexural distance from the plume axis. Elastic flexure is progressively taken up by the vertical viscous flow exerted by the plume, at a time that depends on the visco-elastic relaxation time of the medium. With effective viscosity varying by several orders of magnitudes in the 600–900 °C range (at 45–75 km depth depending on lithospheric thermal age), this relaxation time is found to last between 5 to 10 My for oceanic lithospheres older than 30 My. This time exceeds the time necessary for virgin lithosphere to drift above the plume axis. Therefore we explain the offset of volcanism upstream from the plume axis above La Réunion. We also discuss a similar process at Hawaii (e.g., the presence of Big Island upstream from the plume axis). We suggest that it also applies to the Canaries and Madera hotspots where volcanic islands are dispersed in a 200 km wide band centered along the hotspot tracks (Geldmacher et al., 2005).

We also infer that lithospheric flexure above the plume leads to the formation of melt reservoirs at intermediate lithospheric depth (i.e., 30–40 km, as inferred from seismic tomography below La Réunion) where the plate curvature changes ∼150 km away from the plume axis. Once a primary pathway for magmatic fluids has been built, the progressive growth of the volcanic edifice exerts an increasing downward flexure of opposite curvature to the upward flexure exerted by the plume head. Both flexures being offset by $\alpha \sim 170$ km, the tensile stress due to the edifice actually sucks up and favors further accumulation of magma along the same pathway, so that it stabilizes and eventually drives melt up to 15 km depth. We propose that mechanical weakening associated to such processes explains the apparent low elastic thickness of the lithosphere below Hawaii and la Réunion. Future work aims at analyzing in detail the timing and type of volcanism at la Réunion in conjunction with the evolving stress pattern in the top 30 km of the island.

Acknowledgements

S. Medvedev is thanked for helping out with aesthetics, and anonymous reviewers for strengthening our initial manuscript towards further implications. This work was partially funded by the CNRS–INSU/ALEAS research program.

Appendix A

Hafner's (1951) elastic stress solutions for a plate submitted to a basal shear and normal load, with shear load $q_s = B \cdot \cos(kx)$ where magnitude $B = 0.5A$ is half the applied normal load. These figures display the isocontours of maximum and minimum compressive stresses (top panel), and the associated orientation of potential faults in domains that exceed the Coulomb yield failure criterion (bottom panel). Converging arrows in the bottom central area indicate the domain of compression, which is thus also predicted not to fail. This is exactly the domain of compression in which we are interested in the present study.

Appendix B. Numerical method and parametrization

We use the code Parovoz (Poliakov et al., 1993), based on the numerical method FLAC (Fast Lagrangian Analysis of Continua, Cundall and Board, 1988). This method uses the dynamic relaxation method to model dynamic or static problems, and allows the use of non-linear constitutive laws. Parovoz explicitly resolves the Newtonian dynamic equations of motion (Eq. (B.1)) and the heat transport equation (Eq. (B.2)) in a Lagrangian formulation.

$$\rho g + \frac{\partial \sigma_{ij}}{\partial x_j} = \rho \frac{DV_i}{Dt}, \tag{B.1}$$

with ρ, g, V_i, σ_{ij} being the density, gravity acceleration, velocity vector, and stress tensor components respectively.

$$\frac{\partial T}{\partial t} = \chi \frac{\partial^2 T}{\partial x_i^2} - V_i \cdot \frac{\partial T}{\partial x_i} - V_z \cdot \frac{\alpha g T}{Cp} + \tau \cdot \dot{\varepsilon} + \frac{H_r}{\rho C_p} \tag{B.2}$$

where T is temperature, X is thermal diffusion, C_p is heat capacity, H_r is internal heat production. The first and second terms in Eq. (B.2) describe diffusion and advection, respectively. Advection is actually solved implicitly by the displacement of the Lagrangian mesh. The two following terms describe the adiabatic contribution, approximated using the vertical velocity V_z, and shear heating, product of the non-elastic shear-strain and shear stress, respectively. The last term accounting for radioactive heating is neglected here.

Since large strains require to remesh this grid, inherent errors due to remeshing are reduced with the implementation of passive markers (details in Dorbath et al., 2008), which track evolving pressures and temperatures. Densities depend on temperature and pressure variations (state equation), according to heat expansion and compressibility coefficients α, β, which are assumed to remain constant here:

$$\rho = \rho_0 \cdot \left[1 - \alpha(T - T_0) + \beta(P - P_0)\right]. \tag{B.3}$$

Constitutive equations relate stress and strain primarily by the Maxwell visco-elastic relation (Eq. (B.4)), involving the elastic shear

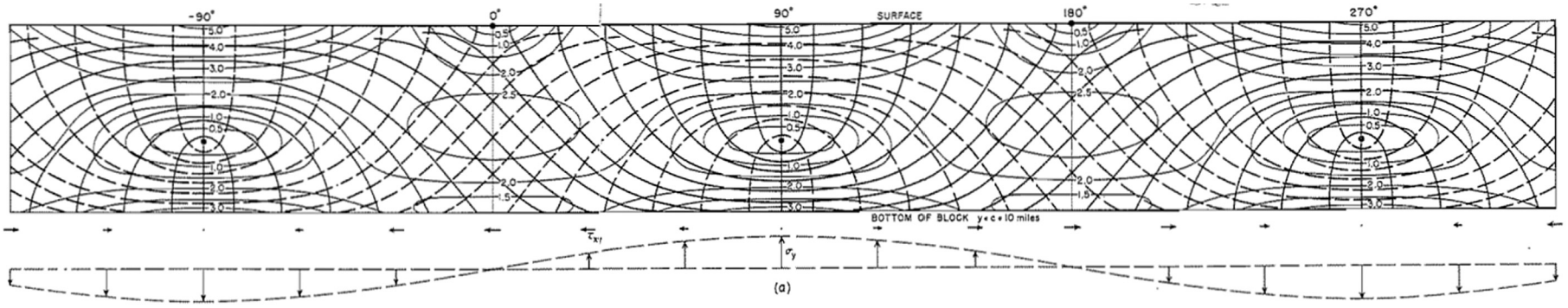

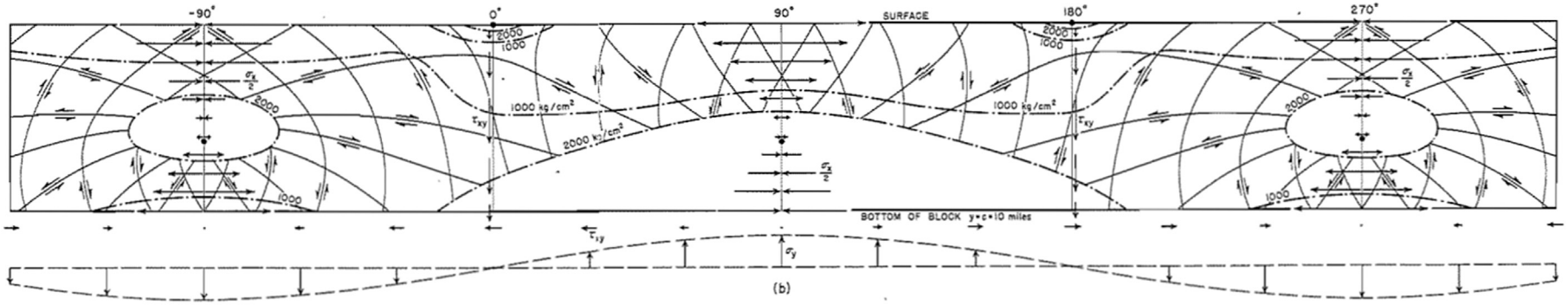

BOUNDARY STRESSES ALONG BOTTOM OF BLOCK:

$\sigma_y = -A \sin \alpha x$;

$\tau_{xy} = -B \cos \alpha x$; $A = 2B$

A_{max} = 1000 to 2000 kg/cm²

LEGEND

(a) — = Trajectories of maximum principal pressure = σ_{min}

(a) – – = " " " minimum " " = σ_{max}

(a) 0.5 = Lines of equal maximum shearing stress = τ_{max} for B = 1.0

(b) = = Position of potential fault surfaces; $\theta = 30°$

(b) – · – = Boundaries of areas of stability for various values of A_{max}

● = Points of zero shearing stress

D

SUPPLEMENTARY STRESS SYSTEM CONSISTING OF
VARIABLE VERTICAL AND SHEARING STRESS ALONG BOTTOM OF BLOCK
WAVELENGTH 62.8 MILES; A=2B

Table B.1
Symbols and parameters used in the numerical plume models (Section 3).

Symbol	Description	Value-units
g	Gravity	9.81 m^2/s
ρ	Reference density	3300 kg/m^3
G, λ	Lamé elastic constants	50–80 GPa
φ, S_0	Friction angle and cohesion for Coulomb failure	10 MPa, 30°
μ_{min}	Minimum bulk viscosity cutoff	$6 \cdot 10^{19}$ Pa s
α_v	Reference thermal expansion	$3 \cdot 10^{-5}$/K
C_p	Reference heat capacity	1250 J/kg/C
k	Reference thermal conductivity	3.3 W/m/°C
A	Lithospheric thermal age	30–70–100 My
Tpl	Plume temperature	+300–400 °C
A, n, Q	Dislocation creep pre-exp. factor, power, activation energy	–
Q^*	$Q^* = 535$: $Q = 535$ kJ/mol, $n = 3.6$, $A = 2.9 \times 10^4$ MPa^{-n}/s	Chopra and Paterson (1984)
	$Q^* = 520$: $Q = 520$ kJ/mol, $n = 3$, $A = 10^4$ MPa^{-n}/s	Burov and Guillou-Frottier (2005)
Peierls	$Ap = 525$ kJ/mol, $\varepsilon p = 5.7e{-}11/s$, $\sigma p = 8.5$ GPa	Kameyama et al. (1999)

modulus G and the effective viscosity η_{eff}. We assume plane-strain and Poissons' ratio $\nu = 0.25$ in order to satisfy the condition of zero mechanical deformation upon initial loading at lithostatic equilibrium.

$$\dot{\varepsilon}_{ij} = \frac{\dot{\tau}_{ij}}{2G} + \frac{\tau_{ij}}{\eta_{eff}}. \tag{B.4}$$

Brittle failure occurs according to a non-associative plastic flow law when the Mohr–Coulomb yield stress τ_y is reached, function of cohesion C and friction φ:

$$\tau_y = C - \tan\varphi \cdot \sigma_n. \tag{B.5}$$

Effective Newtonian viscosity η_{eff} is evaluated according to the temperature- and strain rate-dependent creep flow law (Eq. (B.6)), using the second invariant of the strain-rate tensor ($\dot{\varepsilon}_{II}$), temperature and rock type parameters: A the pre-exponential factor, n the power law exponent and Q the activation energy (given in Table B.1). Note that here activation volume $\upsilon = 0$ according to the chosen laws (cf. main text references):

$$\eta_{eff} = A^{1/n} \cdot \dot{\varepsilon}_{II}^{1/n-1} \cdot \exp\big((Q + P\upsilon)/nRT\big). \tag{B.6}$$

Peierls Mechanism is tested in the last numerical case M8, and is prescribed to occur below 800 °C (as in Zhong and Watts, 2013). The effective viscosity is expressed as:

$$\eta_{eff\ Peierls} = \frac{\sigma_p}{\dot{\varepsilon}_{II}} \cdot \left(1 - \sqrt{\frac{-RT\ln(\dot{\varepsilon}_{II}/A_p)}{\varepsilon_p}}\right).$$

References

d'Acremont, E., Leroy, S., Burov, E.B., 2003. Numerical modeling of a mantle plume: the plume head–lithosphere interaction in the formation of an oceanic large igneous province. Earth Planet. Sci. Lett. 206, 379–396.

Afonso, J.C., Fernández, M., Ranalli, G., Griffin, W.L., Connolly, J.A.D., 2008. Integrated geophysical–petrological modeling of the lithosphere and sublithospheric upper mantle: methodology and applications. Geochem. Geophys. Geosyst. 9 (5).

Ballmer, M.D., Ito, G., Wolfe, C.J., Solomon, S.C., 2013. Double layering of a thermochemical plume in the upper mantle beneath Hawaii. Earth Planet. Sci. Lett. 376, 155–164.

Barruol, G., Fontaine, F.R., 2013. Mantle flow beneath La Réunion hotspot track from SKS splitting. Earth Planet. Sci. Lett. 362, 108–121.

Bass, J.D., 1995. Elasticity of minerals, glasses, and melts. In: Mineral Physics and Crystallography: A Handbook of Physical Constants, vol. 2, pp. 45–63.

Bercovici, D., Karato, S.I., 2003. Whole-mantle convection and the transition-zone water filter. Nature 425, 39–44.

Bercovici, D., Ricard, Y., Schubert, G., 2001. A two-phase model for compaction and damage: 1. General theory. J. Geophys. Res., Solid Earth 106 (B5), 8887–8906.

Bianco, T.A., Ito, G., Becker, J.M., Garcia, M.O., 2005. Secondary Hawaiian volcanism formed by flexural arch decompression. Geochem. Geophys. Geosyst. 6 (8). http://dx.doi.org/10.1029/2005GC000945.

Bonneville, A., Barriot, J.P., Bayer, R., 1988. Evidence from geoid data of a hotspot origin for the southern Mascarene Plateau and Mascarene Islands (Indian Ocean). J. Geophys. Res. 93 (B5), 4199–4212.

Burov, E.B., Diament, M., 1995. The effective elastic thickness (Te) of continental lithosphere: what does it really mean? J. Geophys. Res. 100 (B3), 3905–3927.

Burov, E., Guillou-Frottier, L., 2005. The plume head–continental lithosphere interaction using a tectonically realistic formulation for the lithosphere. Geophys. J. Int. 161 (2), 469–490.

Calmant, S., Francheteau, J., Cazenave, A., 1990. Elastic layer thickening with age of the oceanic lithosphere: a tool for prediction of the age of volcanoes or oceanic crust. Geophys. J. Int. 100 (1), 59–67.

Ceuleneer, G., Rabinowicz, M., 1993. Mantle flow and melt migration beneath oceanic ridges: models derived from observations in ophiolites. In: Mantle Flow and Melt Generation at Mid-Ocean Ridges, pp. 123–154.

Chopra, P., Paterson, M., 1984. The role of water in the deformation of dunite. J. Geophys. Res. 89, 7861–7876.

Cundall, P.A., Board, M., 1988. A microcomputer program for modelling large strain plasticity problems. In: Swoboda, G. (Ed.), Numerical Methods in Geomechanics. Balkema, Rotterdam, pp. 2101–2108.

Dorbath, C., Gerbault, M., Carlier, G., Guiraud, M., 2008. Double seismic zone of the Nazca plate in northern Chile: high-resolution velocity structure, petrological implications, and thermomechanical modeling. Geochem. Geophys. Geosyst. 9 (7). http://dx.doi.org/10.1029/2008GC002020.

Fleitout, L., Yuen, D.A., 1984. Secondary convection and the growth of the oceanic lithosphere. Phys. Earth Planet. Inter. 36 (3), 181–212.

Fontaine, F.R., Barruol, G., Tkalčić, H., Wölbern, I., Rümpker, G., Bodin, T., Haugmard, M., 2015. Crustal and uppermost mantle structure variation beneath La Réunion hotspot track. Geophys. J. Int. 203 (1), 107–126.

Gallart Muset, J., Driad, L., Charvis, P., Sapin, M., Hirn, A., Díaz Cusí, J., Sachpazi, M., 1999. Perturbation to the lithosphere along the hotspot track of La Réunion from an offshore-onshore seismic transect. J. Geophys. Res. 104, 2895–2908.

Geldmacher, J., Hoernle, K., Bogaard, P., Duggen, S., Werner, R., New Geldmacher, J., Hoernle, K., Bogaard, P., Duggen, S., Werner, R., 2005. New 40 Ar/39 Ar age and geochemical data from seamounts in the Canary and Madeira volcanic provinces: support for the mantle plume hypothesis. Earth Planet. Sci. Lett. 237 (1), 85–101.

Gerbault, M., Poliakov, A.N., Daignieres, M., 1998. Prediction of faulting from the theories of elasticity and plasticity: what are the limits? J. Struct. Geol. 20 (2), 301–320.

Gerbault, M., Cappa, F., Hassani, R., 2012. Elasto-plastic and hydromechanical models of failure around an infinitely long magma chamber. Geochem. Geophys. Geosyst. 13. http://dx.doi.org/10.1029/2011GC003917.

Gillot, P.Y., Lefèvre, J.C., Nativel, P.E., 1994. Model for the structural evolution of the volcanoes of Réunion Island. Earth Planet. Sci. Lett. 122 (3), 291–302.

Hafner, W., 1951. Stress distributions and faulting. Geol. Soc. Am. Bull. 62 (4), 373–398.

Hanyu, T., Clague, D.A., Kaneoka, I., Dunai, T.J., Davies, G.R., 2005. Noble gas systematics of submarine alkalic lavas near the Hawaiian hotspot. Chem. Geol. 214, 135–155.

Herzberg, C., Asimow, P., 2015. PRIMELT3 MEGA.XLSM software for primary magma calculation: peridotite primary magma MgO contents from the liquidus to the solidus. Geochem. Geophys. Geosyst. 16 (2), 563–578.

Kameyama, M., Yuen, D.A., Karato, S.I., 1999. Thermal-mechanical effects of low-temperature plasticity (the Peierls mechanism) on the deformation of a viscoelastic shear zone. Earth Planet. Sci. Lett. 168 (1), 159–172.

Kelemen, P.B., Hirth, G., Shimizu, N., Spiegelman, M., Dick, H., 1997. A review of melt migration processes in the adiabatically upwelling mantle beneath oceanic spreading ridges. Philos. Trans. R. Soc. Lond. A 355, 283–318.

Lambeck, K., Penney, C.L., Nakiboglu, S.M., Coleman, R., 1984. Subsidence and flexure along the Pratt–Welker seamount chain. J. Geodyn. 1 (1), 29–60.

Lyakhovsky, V., Ben-Zion, Y., 2014. Damage–breakage rheology model and solid-granular transition near brittle instability. J. Mech. Phys. Solids 64, 184–197.

McDougall, Chamalaun, 1969. Isotopic dating and geomagnetic polarity studies on volcanic rocks from Mauritius, Indian Ocean. Geol. Soc. Am. Bull. 80 (8), 1419–1442.
McNutt, M.K., Ménard, H.W., 1982. Constraints on yield strength in the oceanic lithosphere derived from observations of flexure. Geophys. J. Int. 71 (2), 363–394.
Ménand, T., Daniels, K.A., Benghiat, P., 2010. Dyke propagation and sill formation in a compressive tectonic environment. J. Geophys. Res. 115. http://dx.doi.org/10.1029/2009JB006791.
Michon, L., Ferrazzini, V., Di Muro, A., Villeneuve, N., Famin, V., 2015. Rift zones and magma plumbing system of Piton de la Fournaise volcano: how do they differ from Hawaii and Etna? J. Volcanol. Geotherm. Res. 303, 112–129.
Monnereau, M., Rabinowicz, M., Arquis, E., 1993. Mechanical erosion and reheating of the lithosphere: a numerical model for hotspot swells. J. Geophys. Res., Solid Earth 98 (B1), 809–823.
Moore, J., White, W.M., Paul, D., Duncan, R.A., Abouchami, W., Galer, S.J.G., 2011. Evolution of shield-building and rejuvenescent volcanism of Mauritius. J. Volcanol. Geotherm. Res. 207, 47–66.
Morgan, W.J., 1981. Hotspot tracks and the opening of the Atlantic and Indian oceans. In: The Sea, Ideas and Observations on Progress in the Study of the Seas, vol. 7, pp. 443–487.
Poliakov, A.N.B., Cundall, P.A., Podladchikov, Y.Y., Lyakhovsky, V.A., 1993. An explicit inertial method for the simulation of viscoelastic flow: an evaluation of elastic effects on diapiric flow in two-and three-layers models. In: Flow and Creep in the Solar System: Observations, Modeling and Theory. Springer, Netherlands, pp. 175–195.
Rabinowicz, M., Ceuleneer, G., 2005. The effect of sloped isotherms on melt migration in the shallow mantle: a physical and numerical model based on observations in the Oman ophiolite. Earth Planet. Sci. Lett. 229, 231–246.
Rabinowicz, M., Bystricky, M., Schmocker, M., Toplis, M.J., Rigo, A., Perfettini, H., 2010. Development of fluid veins during deformation of fluid-rich rocks close to the brittle–ductile transition: comparison between experimental and physical models. J. Petrol. 51 (10), 2047–2066.
Ribe, N.M., Christensen, U.R., 1999. The dynamical origin of Hawaiian volcanism. Earth Planet. Sci. Lett. 171 (4), 517–531.
Robinson, E.M., Parsons, B., Driscoll, M., 1988. The effect of a shallow low-viscosity zone on the mantle flow, the geoid anomalies and the geoid and depth-age relationships at fracture zones. Geophys. J. Int. 93 (1), 25–43.
Rubin, A.M., 1995. Propagation of magma-filled cracks. Annu. Rev. Earth Planet. Sci. 23 (1), 287–336.
Sandwell, D., Fialko, Y., 2004. Warping and cracking of the Pacific plate by thermal contraction. J. Geophys. Res. 109. http://dx.doi.org/10.1029/2004JB003091.
Schmeling, H., Marquart, G., 1993. Mantle flow and the evolution of the lithosphere. Phys. Earth Planet. Inter. 79, 241–267.
Schmocker, M., Bystricky, M., Kunze, K., Burlini, L., Stünitz, H., Burg, J.P., 2003. Granular flow and Riedel band formation in water-rich quartz aggregates experimentally deformed in torsion. J. Geophys. Res. 108 (B5).
Sleep, N.H., 1992. Hotspot volcanism and mantle plumes. Annu. Rev. Earth Planet. Sci. 20, 19.
Stixrude, L., Lithgow-Bertelloni, C., 2005. Thermodynamics of mantle minerals—I. Physical properties. Geophys. J. Int. 162 (2), 610–632.
Stuart, W.D., Foulger, G.R., Barall, M., 2007. Propagation of the Hawaiian-Emperor volcano chain by Pacific plate cooling stress. Spec. Pap., Geol. Soc. Am. 430, 497–506.
Thoraval, C., Tommasi, A., Doin, M.P., 2006. Plume-lithosphere interaction beneath a fast moving plate. Geophys. Res. Lett. 33 (1).
Walter, M., 1998. Melting of garnet peridotite and the origin of komatiite and depleted lithosphere. J. Petrol. 39, 29–60.
Watanabe, T., Masuyama, T., Nagaoka, K., Tahara, T., 2002. Analog experiments on magma-filled cracks: competition between external stresses and internal pressure. Earth Planets Space 54 (12), e1247–e1261.
Watson, S., McKenzie, D., 1991. Melt generation by plumes: a study of Hawaiian volcanism. J. Petrol. 32 (3), 501–537.
Watts, A.B., Zhong, S., 2000. Observations of flexure and the rheology of oceanic lithosphere. Geophys. J. Int. 142 (3), 855–875.
Wech, A.G., Thelen, W., 2015. Linking magma transport structures at Kīlauea volcano. Geophys. Res. Lett. 42 (17), 7090–7097.
Zhong, S., Watts, A.B., 2002. Constraints on the dynamics of mantle plumes from uplift of the Hawaiian islands. Earth Planet. Sci. Lett. 203 (1), 105–116.
Zhong, S., Watts, A.B., 2013. Lithospheric deformation induced by loading of the Hawaiian islands and its implications for mantle rheology. J. Geophys. Res. 118 (11), 6025–6048.